



## Alkaline deoxygenated graphene oxide for supercapacitor applications: An effective green alternative for chemically reduced graphene

Sanjaya D. Perera <sup>a</sup>, Ruperto G. Mariano <sup>a</sup>, Nour Nijem <sup>b</sup>, Yves Chabal <sup>b</sup>, John P. Ferraris <sup>a</sup>, Kenneth J. Balkus Jr. <sup>a,\*</sup>

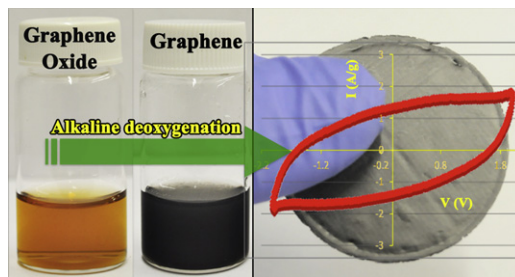
<sup>a</sup> Department of Chemistry and The Alan G. MacDiarmid Nanotech Institute, 800 West Campbell Rd, The University of Texas at Dallas, Richardson, TX 75080, USA

<sup>b</sup> Laboratory for Surface and Nanostructure Modification, Department of Material Science and Engineering, 800 West Campbell Rd, The University of Texas Dallas, Richardson, TX 75080, USA

### HIGHLIGHTS

- Novel green method to prepare graphene for supercapacitors without hazardous reducing agents.
- An alkaline deoxygenation route was developed to fabricate binder-free, flexible electrodes.
- Electrochemical properties of paper electrodes show high power and energy densities.
- This method to prepare graphene from graphene oxide may facilitate energy storage applications.

### GRAPHICAL ABSTRACT



### ARTICLE INFO

#### Article history:

Received 17 February 2012

Received in revised form

19 April 2012

Accepted 20 April 2012

Available online 3 May 2012

#### Keywords:

Graphene

Graphene oxide

Reduced graphene oxide

Supercapacitors

### ABSTRACT

Graphene is a promising electrode material for energy storage applications. The most successful method for preparing graphene from graphite involves the oxidation of graphite to graphene oxide (GO) and reduction back to graphene. Even though different chemical and thermal methods have been developed to reduce GO to graphene, the use of less toxic materials to generate graphene still remains a challenge. In this study we developed a facile one-pot synthesis of deoxygenated graphene (hGO) via alkaline hydrothermal process, which exhibits similar properties to the graphene obtained via hydrazine reduction (i.e. the same degree of deoxygenation found in hydrazine reduced GO). Moreover, the hGO formed freestanding, binder-free paper electrodes for supercapacitors. Coin cell type (CR2032) symmetric supercapacitors were assembled using the hGO electrodes. Electrochemical characterization of hGO was carried out using lithium bis(trifluoromethanesulfonyl)imide (LiTFSI) and ethylmethylimidazolium bis-(trifluoromethanesulfonyl)imide (EMITFSI) electrolytes. The results for the hGO electrodes were compared with the hydrazine reduced GO (rGO) electrode. The hGO electrode exhibits a energy density of  $20 \text{ W h kg}^{-1}$  and  $50 \text{ W h kg}^{-1}$  in LiTFSI and EMITFSI respectively, while delivering a maximum power density of  $11 \text{ kW kg}^{-1}$  and  $14.7 \text{ kW kg}^{-1}$  in LiTFSI and EMITFSI, respectively.

© 2012 Elsevier B.V. All rights reserved.

### 1. Introduction

The interest in supercapacitors for next generation energy storage devices due to their high power and energy densities continues to grow [1–4]. They are essentially intermediate energy storage systems that possess higher power densities than batteries

\* Corresponding author. Tel.: +1 972 883 2659; fax: +1 972 883 2925.

E-mail address: [Balkus@utdallas.edu](mailto:Balkus@utdallas.edu) (K.J. Balkus).

and higher energy densities than conventional dielectric capacitors. Supercapacitors are generally of two varieties based on the charge storage mechanism: surface ion adsorption (electrochemical double layer capacitors, EDLC) and redox reactions (pseudocapacitance). In EDLC, capacitance comes from the charges stored at the electrode/electrolyte interface. Pseudocapacitance mainly arises from reversible faradaic redox reactions that take place within the material. Carbon is the most common electrode material for EDL capacitors. The stability of carbon materials over large voltage ranges and the low production cost make them attractive for commercial energy storage applications. Activated carbon (AC) is employed in many commercially available EDL supercapacitors [5,6]. However, AC electrodes require binding materials such as acetylene black to prepare the electrodes. The binder adds weight, limits access to the electrode porosity and can result in agglomeration which all effect the performance of these electrodes [7]. Carbon nanotubes (CNTs) have very high surface areas and exhibit stable EDL properties but the specific capacitance of CNT electrodes is limited ( $\sim 25 \text{ F g}^{-1}$ ) [8,9]. In order to overcome these limitations, the CNTs are often combined with conducting polymers or metal oxides, which exhibit pseudocapacitance behavior. Such CNT hybrids shown improved power and energy density performance [10–12]. We have fabricated CNT/V<sub>2</sub>O<sub>5</sub> nanowire binder-free paper electrodes, which exhibit balanced EDL and pseudocapacitance activity [13]. Generally, compared to EDLC, most electroactive metal oxide based electrodes greatly deviate from the ideal capacitive behavior at higher operational voltages and require slow charging and discharging. Even though CNT/V<sub>2</sub>O<sub>5</sub> electrodes have shown promise, the high processing cost of CNTs and purification may significantly limit the commercialization of CNT based supercapacitors. In recent years, graphene has attracted attention as an electrode material in part because of a high theoretical surface area (2630 m<sup>2</sup> g<sup>-1</sup>), excellent electron mobility (250,000 cm<sup>2</sup> V s<sup>-1</sup>) and good mechanical strength (1 TPa) [14]. Unlike CNTs, flake graphite is naturally abundant and requires much lower processing costs to make graphene. Vivekchand et al. reported the electrochemical performance of chemically reduced graphene as an electrode material for supercapacitors [15]. Ruoff and coworkers measured a specific capacitance of 135 F g<sup>-1</sup> and 99 F g<sup>-1</sup> for graphene in aqueous and organic electrolyte respectively [16]. Chen and coworkers also studied the EDL capacitive behavior of graphene in an aqueous KOH and observed a specific capacitance of 205 F g<sup>-1</sup> [17]. Yang and coworkers prepared high voltage supercapacitors using hydrated graphene films in neutral aqueous electrolyte at a maximum voltage of 1.6 and 1.8 V [18]. Graphene has also been utilized to fabricate ultrathin, flexible electrodes for bendable power sources [19,20].

One of the challenges for graphene is the processing of graphite. Strong van der Waals interactions exist in naturally occurring graphitic flakes making them hydrophobic and insoluble in most common solvent systems. Different approaches have been developed to exfoliate naturally occurring graphite flakes to obtain individual or few layers of graphene [21–24]. Among these techniques chemical exfoliation of graphite to form individual graphene oxide (GO) layers using strong oxidizing agents has become the most common technique [25]. Unfortunately, GO exhibits poor electronic conductivity due to the interruption of conjugation by substituted oxygen functional groups. Various reducing agents such as N<sub>2</sub>H<sub>4</sub> [26], NaBH<sub>4</sub> [27] and alcohols [28] have been used to restore the sp<sup>2</sup> network of highly conducting graphene. Most of the chemical reducing agents commonly used are hazardous or generate hazardous byproducts. Moreover, hydrazine reduced graphene tends to irreversibly agglomerate and convert back to graphite. There is a challenge to identifying alternative *green* approaches that use non-toxic chemicals to produce graphene on a large-scale.

It has previously been reported that the deoxygenation of GO occurs under alkaline conditions [29,30]. To date this non-toxic approach to prepare graphene has not been explored for the preparation of electrodes for energy storage. In the present study graphene was prepared by alkaline hydrothermal synthesis and studied as electrodes for symmetric supercapacitors. Moreover, we prepared *binder-free flexible* graphene papers using this novel *green* method and fabricated coin cell type supercapacitors. Since the hydrazine reduced graphene has been studied as an electrode material, we systematically compared the performance of hGO and rGO electrodes using lithium bis(trifluoromethanesulfonyl)imide (LiTFSI) in acetonitrile as the electrolyte. Electrolyte solutions based on aprotic solvents, typically acetonitrile, can operate at room temperature with a maximum cell voltage of 2.5–3.0 V. Additionally, the electrochemical stability of organic solvents decreases by increasing temperature and the cycle life of the cell drastically decreases with increasing the maximum cell voltage window [31]. To increase the operational voltage window of supercapacitors, the electrode performance of both types of graphene was evaluated in the ionic liquid electrolyte ethylmethylimidazolium bis(trifluoromethanesulfonyl)imide (EMITFSI), which is stable over the potential range of 0–4 V. The power and energy density performance of deoxygenated GO in organic and ionic liquid electrolytes were comparable to the hydrazine reduced GO (rGO). The electrochemical properties of hGO suggest that the alkaline hydrothermal synthesis is an effective green approach and alternative to the conventional hydrazine reduction of GO for supercapacitors.

## 2. Experimental

### 2.1. Materials

Graphite powder was purchased from Sigma Aldrich. H<sub>2</sub>SO<sub>4</sub> (EMD chemicals), HCl, NaOH (Fischer Scientific), NaNO<sub>3</sub> (Sigma Aldrich) and KMnO<sub>4</sub> (Baker analyzed) were used as received. Lithium bis(trifluoromethanesulfonamide) (LiTFSI) was obtained from TCI America while ethylmethylimidazolium bis(trifluoromethanesulfonyl)imide (EMITFSI) was obtained from EMD chemicals.

### 2.2. Characterization

X-ray powder diffraction (XRD) patterns were obtained using a Rigaku Ultima IV diffractometer (Cu K<sub>α</sub> radiation). Raman spectra were collected using a JY Horiba HR-800 spectrophotometer. Transmission electron microscope (TEM) and scanning electron microscope (SEM) images were obtained using a JEOL JEM-2100 TEM at 200 kV (JEOL Co. Ltd.) and a Leo 1530 VP field emission electron microscope respectively. X-ray photoelectron spectroscopy (XPS) measurements were performed *ex situ*, using a Perkin Elmer PHI System. The photoelectrons were excited using monochromatic Al K<sub>α</sub> radiation ( $h\nu = 1486.6 \text{ eV}$ ) and the spectra were acquired with 45° emission angle, using a 0.125 eV step size and a pass energy of 29.35 eV in the hemispherical analyzer. The nominal pressure in the analysis chamber was  $3 \times 10^{-9} \text{ Torr}$ . Cyclic voltammograms (CV) and galvanostatic charge/discharge curves were obtained using Arbin battery testing system (BT2000) within 2.5 V (for LiTFSI) and 3.7 V (for EMITFSI) potential window. Electrochemical impedance spectroscopy (EIS) measurements were performed on computer controlled EG&G Princeton Applied Research potentiostat/galvanostat (model 2273A).

### 2.3. Synthesis of graphene oxide

GO was synthesized using a modified Hummer's method [25]. Briefly, 0.5 g of graphite and 0.5 g of NaNO<sub>3</sub> were mixed in 23 mL of

12.1 M  $\text{H}_2\text{SO}_4$  and stirred in an ice bath for 15 min. Then 4.0 g of  $\text{KMnO}_4$  was slowly added in an ice bath to yield a purple-green mixture. This suspension was transferred to a 40 °C water bath and magnetically stirred for 90 min. The dark brown colored paste was diluted by the slow addition of 50 mL of deionized water (DI) and allowed to stir for a further 10 min. 6 mL of  $\text{H}_2\text{O}_2$  (30%) was slowly added to quench the solution to produce a golden brown sol. A further 50 mL DI water was added to dilute the sol and the resultant product centrifuged and washed with warm DI water repeatedly to adjust the pH to ~6. Finally the product was dried at 80 °C for 24 h.

#### 2.4. Synthesis of hGO

50 mg of GO was sonicated in 50 ml of DI water for 1 h to achieve uniform dispersions of GO. Then 10.5 g of NaOH was added and the mixture was transferred to a Teflon-lined autoclave. The mixture was then heated at 120 °C under static conditions for 24 h. The resulting black colored gel was neutralized with 0.1 M HCl solution. The final product was washed with DI water several times and redispersed in DI water. Finally, the hGO dispersion was suction filtered using Nylon filter paper (Varian Chromatography System-Nylon 66, 0.45  $\mu\text{m}$  pore size and 47 mm in diameter) to make flexible paper electrodes.

#### 2.5. Synthesis of rGO

50 mg of GO were sonicated in 50 ml of DI water for 1 h to obtain a homogeneous dispersion of GO. 50  $\mu\text{l}$  of hydrazine hydrate was added to the dispersion and stirred at 90 °C for 90 min. The dark black suspension was washed repeatedly with DI water and 0.5%  $\text{NH}_3$  solution. Finally the dispersion was suction filtered using Nylon filter paper (Varian Chromatography System-Nylon 66, 0.45  $\mu\text{m}$  pore size and 47 mm in diameter) to make flexible paper electrodes.

#### 2.6. Coin cell type supercapacitor assembly

The coin cell packaging (CR2032) was used to assemble the supercapacitors [13]. Stainless steel spacers in the packaging were used as current collectors. A disk of carbon fiber sheet (Spectracarb

2250) was placed between each stainless steel current collector in order to decrease the contact resistance ( $R_c$ ). The hGO and rGO electrodes were cut into circles (Diameter of 1 cm and total mass loading of two electrodes were ~2 mg). The hGO paper electrodes were separated by Teflon® film and the electrolyte, 0.1 M lithium bis(trifluoromethanesulfonyl)imide (LiTFSI) in dry acetonitrile, was introduced and sealed in the cell using a coin cell crimper (Shenzhen Yongxinye precision machinery mold) by pressing at 1500 psi. The same procedure was used to assemble the cells with rGO electrodes and ionic EMITFSI liquid electrolyte (ethylmethylimidazolium bis(-trifluoromethanesulfonyl)imide) (~120 ppm water content).

### 3. Results and discussion

Graphene oxide was synthesized from graphite flakes by a modified Hummer's method [25]. Fig. 1 shows the XRD patterns of graphite and GO. Pristine graphite flakes exhibit a strong (002) reflection at 26.5° which corresponds to an interlayer distance ( $d$ -spacing) of ~0.34 nm (Fig. 1a). After oxidation of graphite to GO, the (002) diffraction peak shifts to a lower  $2\theta$  angle (10.8°), which corresponds to an interlayer distance of approximately ~0.82 nm. This indicates the GO sheets are separated due to the covalently bonded oxygen [25,32]. The oxidation of graphite to GO disrupts the conjugation of the graphene structure resulting a decrease in electronic conductivity. Hydrazine has been widely used to reduce GO to graphene and restore the conjugated  $\text{sp}^2$  network. It was reported that hydrazine reduced GO exhibit higher electronic conductivities [33] than that of GO and can be used to prepare films and composites with different materials for energy conversion and storage applications [19,20,34–36]. Although hydrazine is the most common reducing agent used to prepare reduced GO, high toxicity and hazardous bi-products greatly limits its use for the large-scale preparation of graphene for industrial applications. The irreversible aggregation of graphene layers in the presence of excess hydrazine has also been reported. In order to overcome these limitations, we prepared deoxygenated GO by an alkaline hydrothermal process (hGO) at 120 °C, which was expected to deoxygenate GO to a higher degree than either just washing or the low temperature alkaline treatment previously reported [29]. Fig. 1a shows the XRD patterns for the hydrazine reduced GO (rGO) and hGO. The interlayer distance of rGO obtained from (002) reflection of the XRD pattern

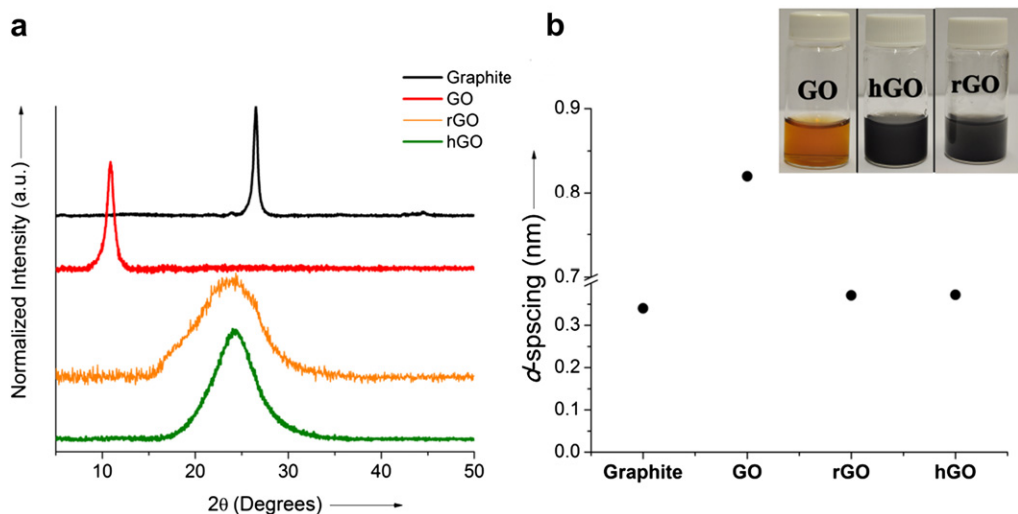


**Fig. 1.** (a) XRD patterns of Graphite after oxidation to GO and followed by the reduction with hydrazine and alkaline hydrothermal treatment. (b)  $d$ -spacing of each samples (digital photographs of aqueous dispersions of GO and hGO sample inset).

at  $23.6^\circ$  was  $\sim 0.37$  nm. The decrease in interlayer spacing between individual graphene sheets is attributed to the van der Waals interaction between  $sp^2$  hybridized carbon frame-work that was restored during the chemical reduction. The XRD pattern of hGO also exhibits a (002) reflection at  $23.9^\circ$  corresponding to the interlayer spacing of  $\sim 0.37$  nm. The broad XRD peak of the hGO suggests these stacked graphene sheets are few layers thick [34]. The change in  $d$ -spacing after the oxidation, reduction and alkaline deoxygenation is summarized in the Fig. 1b. The typical color change from golden brown to dark black was observed after alkaline hydrothermal reaction and hydrazine reduction and hydrazine treatment (Fig. 1b inset). The presence of oxygen functional groups introduced in Hummers method facilitates the homogeneous dispersion of GO in different solvent systems. Unlike graphite flakes, which are a form of aggregated graphene, individual GO surface bears oxygen functionalities such as carboxylates. These functional groups on both sides of GO prevents aggregation and introduce hydrophilic nature to the GO, which helps to suspend individual or few layers of GO in different solvent systems.

The deoxygenation of GO was analyzed by X-ray photoelectron spectroscopy (XPS). The C1s XPS spectra of pristine graphite, GO, rGO and hGO are shown in Fig. 2. The C–C peak for graphite is observed at 284.1 eV. Naturally occurring graphites have only a very small amount of oxygen functional groups. After oxidation the GO C1s XPS spectrum (Fig. 2b) with peaks for C–O ( $\sim 285$  eV) and ( $\sim 289$  eV) C=O oxygen functionalities. Based on the ratio under the area of C–C and C–O peaks, GO is  $\sim 76\%$  oxygen. The C–O peak is mainly due to the hydroxyl and 1, 2 epoxide groups while C=O

peak is mainly due to the carboxyl and ketone groups [26,37]. The deconvoluted XPS spectra of the C1s for rGO and hGO (Fig. 2c, d) show a dramatic decrease in the intensity of C–O species due to the reduction of hydrazine and alkaline deoxygenation respectively. Based on XPS data, the amounts of C–O species in both rGO and hGO are approximately the same ( $\sim 20\%$ ), suggesting that the alkaline hydrothermal treatment is capable of converting GO to graphene as well as hydrazine. However, N atoms from hydrazine can accumulate in rGO and form C–N bonds by removing oxygen atoms. Since N from hydrazine behaves as a donor compensating  $p$ -type holes, the sheet resistance of rGO is higher than graphene prepared with the other chemical reducing agents [27]. XPS survey spectrum of rGO shows the formation of C–N bonds, confirmed by the presence of N 1s peak at 399.8 eV (Fig. s1). Even though the mechanism for the alkaline deoxygenation of the oxygen functional groups on GO is unclear, Wilson et al. concluded that strong alkalines can detach large oxidized debris attached to the GO to yield graphene [30]. Fan and coworkers studied the pH dependency of the alkaline deoxygenation and observed the faster reaction at higher pH [29]. Unlike washing with NaOH and low temperature treatments, the hydrothermal treatment conducted at  $120^\circ\text{C}$  may increase the degree of deoxygenation. During the alkaline hydrothermal treatment in 5 M NaOH the golden brown GO dispersion turns to the dark black color and eventually precipitates. The precipitation of hGO is mainly due to the less hydrophilic nature due to the removal of oxygen functional groups [38].

Raman spectroscopy also reflects the structural and chemical changes of graphite to GO, rGO and hGO. Fig. 3 shows two

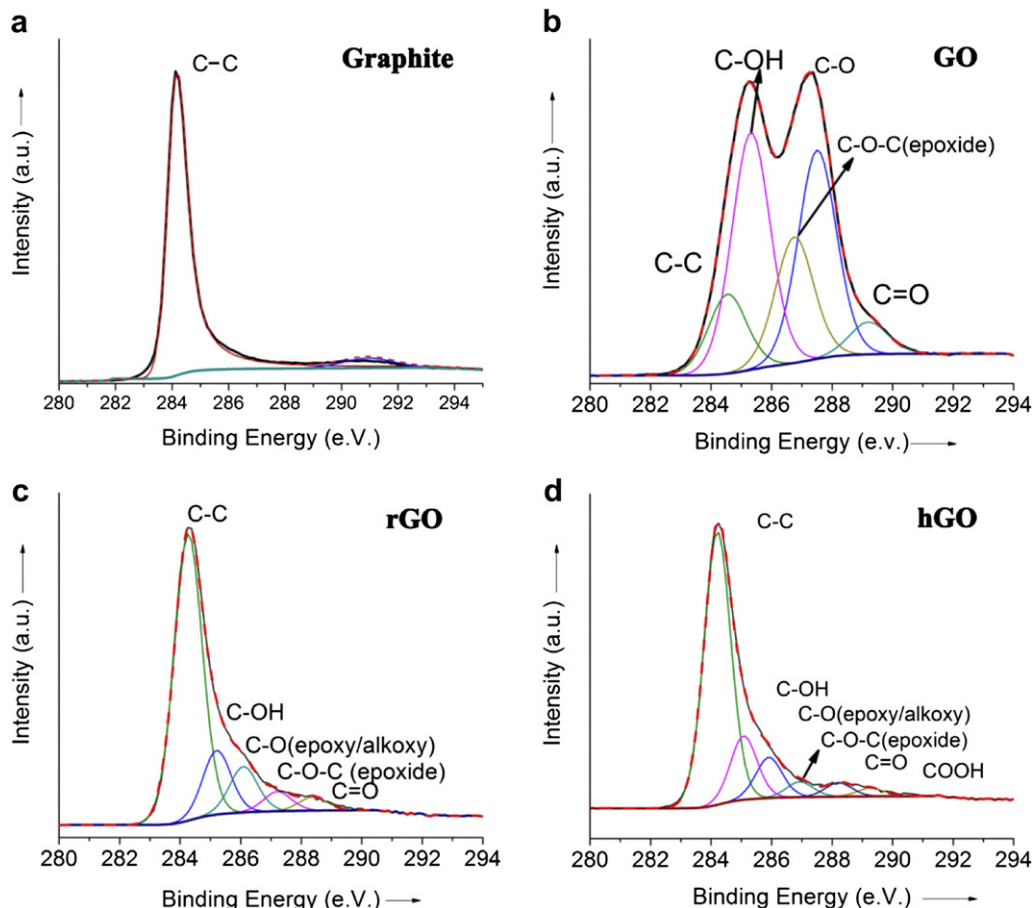


**Fig. 2.** XPS spectra of (a) Graphite, (b) GO, (c) Hydrazine reduced GO and (d) Hydrothermally deoxygenated GO. Deconvoluted C–C and C–O peaks shows relative C:O elemental ratio of GO after chemical modifications.

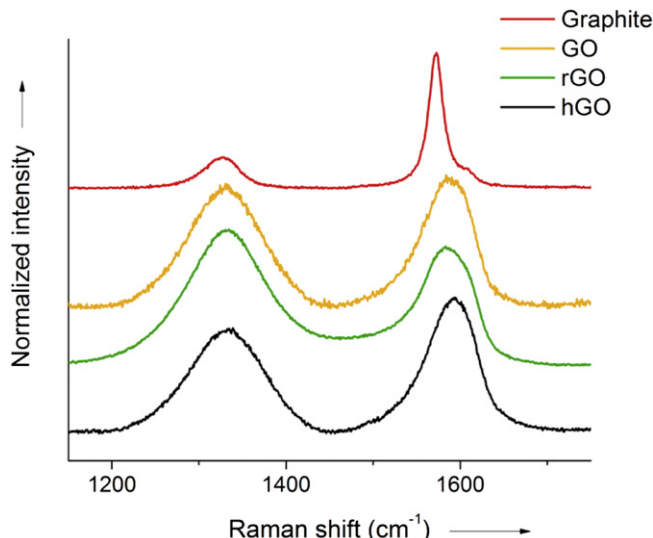


**Fig. 3.** Raman spectra of D and G bands. High intense G band of the hGO sample suggests the presence of low defect level and large  $sp^2$  moieties.

characteristic D and G bands at  $\sim 1300\text{ cm}^{-1}$  and  $\sim 1600\text{ cm}^{-1}$  respectively. The G band originates from in plane vibrations of  $sp^2$  carbons in graphene domains. The D band is related to the edges, defects and structurally disordered carbons found in graphene sheets. The low intensity of the D band for the pristine graphite indicates a low degree of defects due mostly to the sheet edges. Compared to the graphite, the intensity of the D band in GO, rGO and hGO is significantly increased after chemical treatment as different types of structural defects are introduced. Both D and G bands undergo significant changes upon amorphization of graphite, which consists of  $sp^3$  carbons [39]. Disorder and defects in graphite lead to broad the D and G bands, as well as an increase the intensity of the D band [40]. The intensity ratio of D band to G band ( $I_D/I_G$ ) indicates the degree of defects presence in graphene materials. Table 1 summarizes Raman data for graphite, GO, rGO and hGO. Typically, reduced GO displays an increased  $I_D/I_G$  ratio relative to graphite, suggesting a decrease in size of the average  $sp^2$  domains due to the introduction of oxygen functional groups [41–43]. The  $I_D/I_G$  ratio for hGO is lower than that of GO and rGO, indicating the hydrothermally prepared hGO has relatively large  $sp^2$  domains [22,45]. The  $I_D/I_G$  in hGO (0.73) is even lower than the values calculated by Matsumoto et al., who reported  $I_D/I_G$  values (0.98) for the photoreduced GO in the presence of  $\text{Ag}^+$  [46] and thermally reduced GO (1.01) [47]. Planer domain size of graphite microcrystallites ( $L_a$ ) were calculated according to the equation,  $L_a = 44/R$ , where R is  $I_D/I_G$  ratio [48]. As reported in the Table 1, graphite has the highest domain size due to the un interrupted graphite structure. The oxidation of graphite introduces oxygen functional groups and cleaves the large continuous domains to smaller domains ( $\sim 4.73\text{ nm}$ ). The domain size for hGO,  $\sim 6.03\text{ nm}$ , is larger than that of rGO ( $\sim 4.63\text{ nm}$ ). This suggests that, after the alkaline hydrothermal treatment, the size of the undisrupted  $sp^2$  domains of GO

did not change dramatically. Unlike hydrazine reduced GO, the size of the graphene domains in hGO are bigger and exhibit a lower degree of defects. It was previously reported that the smaller average  $sp^2$  domain size in the hydrazine-reduced rGO cleaved the graphene structure to a large number of smaller domains [44,45]. This may also be caused by a decrease in the average size of the  $sp^2$  domains after oxidation relative to the pristine graphite. Since alkaline hydrothermal treatment simply cleaves oxidative debris and does not disrupt the graphene structure, the individual  $sp^2$  domain size is bigger and more preserved than that of rGO. The peak for C–O ( $1581\text{ cm}^{-1}$ ) at the G band was shifted compared with that of graphite ( $1570\text{ cm}^{-1}$ ). This is attributed to the presence of isolated double bonds that resonate at frequencies higher than that of the G band of the graphite [49]. Moreover, compared to graphite, the G band of the hGO is shifted from  $1570\text{ cm}^{-1}$ – $1587\text{ cm}^{-1}$ . The G band shift mainly reflects the presence of large unmodified graphitic carbons and the presence of double bonds. The deconvoluted Raman spectra for hGO and rGO show slightly different carbon species present under the G band as shown in Fig. s2. The G band consists of mainly three bands at  $1534\text{ cm}^{-1}$ ,  $1585\text{ cm}^{-1}$  and  $1606\text{ cm}^{-1}$  which are assigned to amorphous carbons, ideal graphite and graphene sheets [50]. The deconvoluted peak area ratio for graphite: graphite for hGO was  $\sim 1:3$ , while for rGO  $\sim 1:2$ . Both samples contain trace amounts of amorphous carbon. The C:O ratio obtained from XPS data can be directly correlated with the degree of reduction or the lower number of defects. Compared to rGO, the lower degree of defects is presumably due to the lower C:O ratio found in hGO.

### 3.1. Surface morphology of hGO paper electrodes

Conventional graphene electrodes are often prepared by pressing a mixture of graphene powder with organic binders. These nonconducting binders drastically reduce the active surface area and the electronic conductivity of the electrode. Hence, the unique electronic and physical properties of graphene are greatly reduced. Several groups have prepared graphene as hydrogels and binder-free papers [51–53]. The inherent advantage of these types of graphene electrodes over graphene powder/binder electrodes is the interconnected porous network, which facilitates the electrolyte penetration. Graphene paper electrodes perform as well as CNT (carbon nanotube) paper or graphite foils for energy storage [20]. The alkaline hydrothermal conversion of GO to hGO is an inexpensive and green method to deoxygenate GO. Additionally, vacuum filtration generates freestanding graphene paper electrodes. Fig. 4a inset shows a digital photograph of a freestanding hGO flexible paper electrode. This paper can be easily handled and cut into circular shaped electrodes for supercapacitors. In order to compare the morphology and electrochemical properties, rGO paper electrode was also prepared by vacuum filtration. The surfaces of the hGO paper exhibit an irregular morphology, which is common for graphene based paper electrodes (Fig. 4a) [20,22]. In order to obtain high double layer capacitance, the pore structures and surface properties of the electrode are equally important. SEM image of the surface of the hGO paper electrode is usually irregular in shape and individual graphene sheets crumpled to enhance the surface area of the electrode electrolyte interface. The porous layered structure extended along the cross section ( $\sim 10\text{ }\mu\text{m}$  thick) of the freestanding paper electrode is shown in Fig. 4b. Completely exfoliated hGO sheets assembled in the paper electrode create void spaces between the layers, which could greatly contribute to rapid charge and discharge cycles. The transmission electron microscopy (TEM) images of hGO reveal that the hGO are exfoliated and exhibited a lamellar morphology, which are consistent with the SEM images (Fig. 4c). Most of the hGO sheets observed in TEM

**Table 1**  
Comparison of  $I_D/I_G$  intensity ratios and micro crystallite sizes of GO, rGO and hGO

	D band ( $\text{cm}^{-1}$ )	G band ( $\text{cm}^{-1}$ )	$I_D/I_G$	$L_a$ (nm)
Graphite	1315	1570	0.20	22.0
GO	1322	1581	0.93	4.73
rGO	1321	1569	0.95	4.63
hGO	1320	1587	0.73	6.03

analysis are well separated few layers or single layer lamella structures. Moreover, these sheets exhibit layered structures similar to the rGO sheets (Fig. 4d).

### 3.2. Electrochemical characterization – comparison of hGO and rGO

The EDLC behavior of hGO and rGO paper electrodes was evaluated in two electrode symmetric coin cell. First we explored the capacitance properties of the hGO electrode via cyclic voltammetry (CV) within the potential range −1.0 to 1.5 V in 1M LiTFSI in acetonitrile. Fig. 5a shows the CV diagrams for the hGO electrode. The CV curve of hGO is close to being rectangular in shape at scan rates in the range of 10–75 mV s<sup>−1</sup>, indicating quick charging via EDL capacitance for the hGO electrode. Fig. 5b compares the CV diagrams of hGO and rGO acquired at 25 mV s<sup>−1</sup>. Compared to rGO, hGO electrode also exhibits the EDL capacitive behavior similar to that of rGO and previously reported chemical methods [15,21,47].

Galvanostatic charge discharge measurements were performed on the hGO electrodes to evaluate the electrochemical properties over the potential window at different current densities in LiTFSI electrolyte (Fig. 5c). The specific capacitance ( $C_{sp}$ ) was calculated using the gradient of the discharge profile according to the equation  $C_{sp} = (I \times \Delta t) / (m \times \Delta V)$ , where  $I$  is the constant discharge current,  $\Delta t$  is the discharge time,  $m$  is the total mass of the both electrodes and  $\Delta V$  is the voltage difference after the ohmic drop. The calculated specific capacitance of the device with the hGO electrode was 145 F g<sup>−1</sup> and 112 F g<sup>−1</sup> for rGO electrode. The discharge profile for the hGO electrode exhibits a linear shape demonstrating the absence of Faradaic activities. The voltage drop

at the beginning of the discharge was considerably lower even at a higher constant current density of 5 A g<sup>−1</sup>. Based on discharge profiles, energy density and power densities were calculated using the equation  $E = (I \times \Delta t \times \Delta V) / (2 \times m)$  and  $P = \Delta E / \Delta t$ , where  $E$  is the energy density and  $P$  is the power density. Fig. 5d shows the comparison of the discharge curves at 1 A g<sup>−1</sup> for hGO and rGO. At 1 A g<sup>−1</sup> the hGO electrode and rGO electrode delivered 30 W h kg<sup>−1</sup> and 23 W h kg<sup>−1</sup> while maintaining power densities of 1.2 kW kg<sup>−1</sup> for both electrodes. It can be seen that the hGO electrode completely discharges in 85 s while delivering higher energy density than that of rGO. Moreover, The maximum power density of 12.5 kW was recorded for hGO electrode at a discharge rate of 13 A g<sup>−1</sup>. The energy and power density of hydrothermally treated GO is comparable and higher than that of the previously reported values for chemically reduced GO based electrodes [15,54]. The ability of hGO paper electrodes to deliver comparably high energy and power densities in shorter period of time than that of rGO electrode suggests that the hGO electrode has the desirable faster charge discharging properties in Li<sup>+</sup> based electrolyte. The energy and power performance of the hGO electrode suggests that lithium ions are reversibly inserted/extracted in the layers similar intercalation mechanism to that of graphite electrodes [55]. The Faradaic capacity of graphite compounds arises due to the intercalation of lithium ions according to the following equation (Eq (1)) [55,56].



Moreover, Li ions intercalated to the interlayer spacing of the hGO sheets may also facilitate Li ion storage during the charging cycle. The fast charge discharge properties observed in hGO

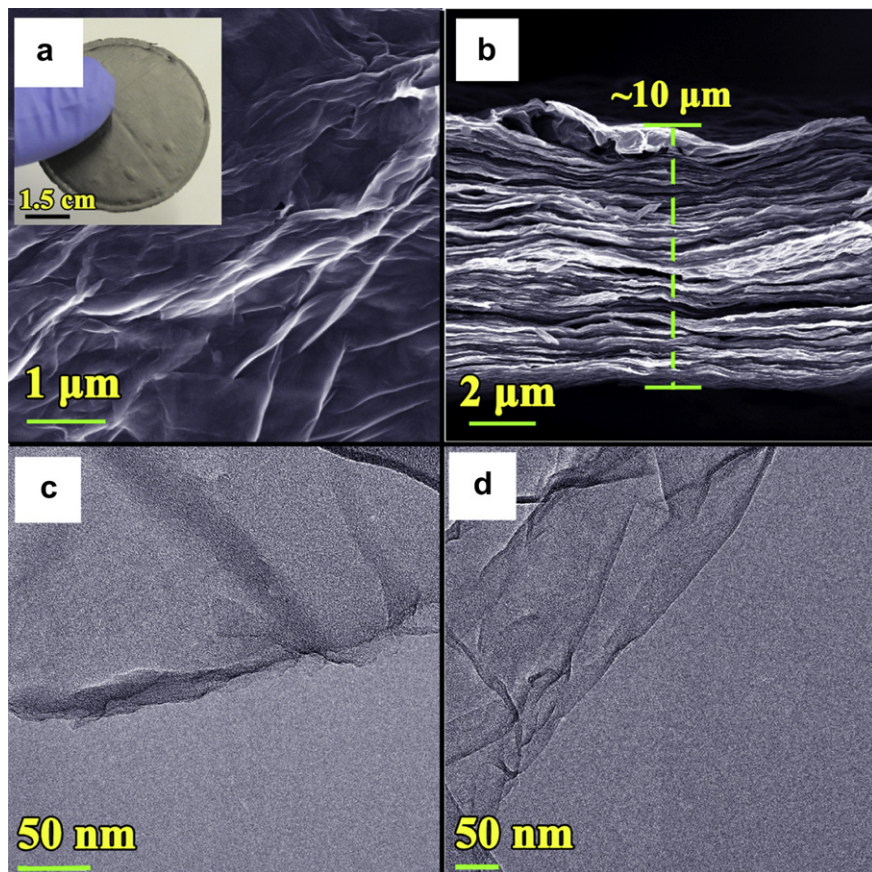


**Fig. 4.** SEM image of the surface of the (a) hGO paper and (b) cross section of the hGO paper. Figure a. inset shows the digital photograph of the binder-free flexible hGO paper. TEM images of the exfoliated hGO (c) and rGO (d) layers.

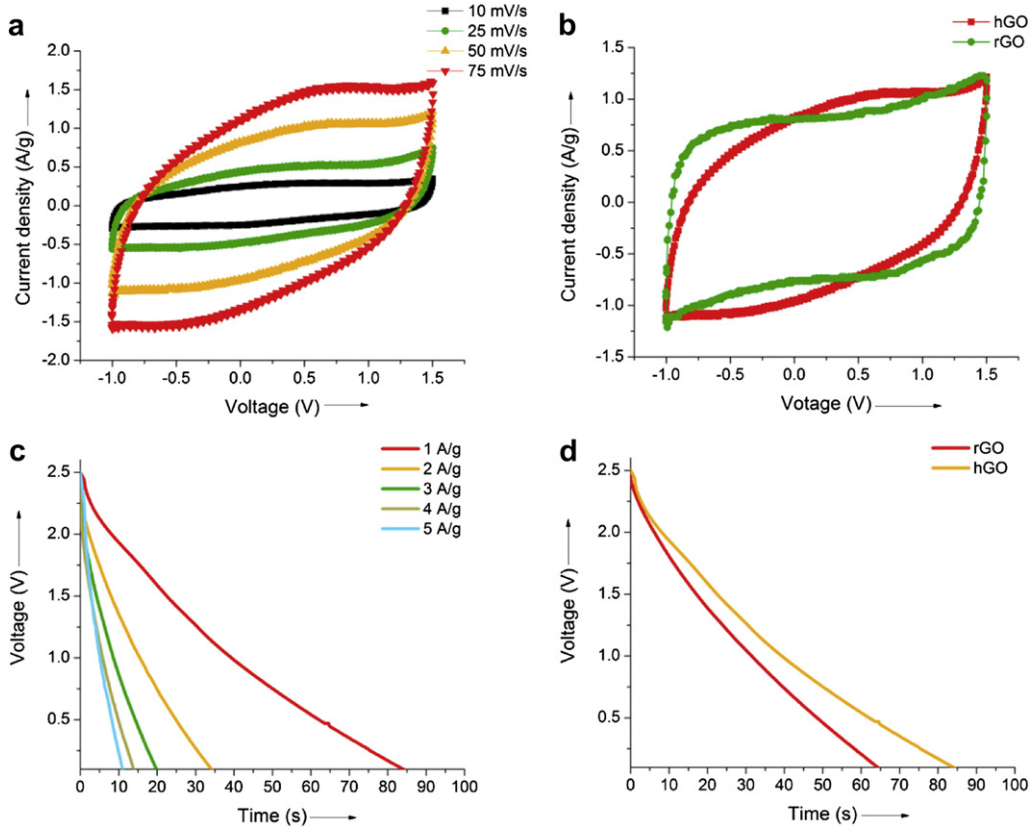


**Fig. 5.** (a) Cyclic voltammograms of the hGO paper electrode for various voltage scan rates in LiTFSI electrolyte. (b) Comparison of cyclic voltammograms of hGO and rGO acquired at  $25 \text{ mV s}^{-1}$ . (c) Galvanostatic discharging curves at various constant current densities and the comparison of discharge curves of hGO and rGO at  $1 \text{ A g}^{-1}$  (d).

electrodes indicate the interlayer spacing of hGO is accessible for Li ion intercalation. However, organic electrolytes limit the potential window and accessible temperature range of energy storage devices. Especially for high energy and power devices, which require larger stable performance over broad temperature ranges. Ionic liquids, which have been widely studied for supercapacitors [31], exhibit very low vapor pressure, high thermal stabilities and wide stable electrochemical windows with good conductivities. The ionic liquid EMITFSI is known to have a stable electrochemically up to 4V [53,57,58]. According to the equation for energy density,  $E = 1/2CV^2$  where, C is the capacitance and V is the voltage, increasing the operational voltage window is greatly beneficial for increasing the energy and power densities. The electrochemical performance of the hGO electrode in an ionic liquid (EMITFSI) electrolyte was investigated using CV and Galvanostatic charge/discharge curves.

Fig. 6a shows the CV diagrams of hGO acquired at 10, 25, 50 and 75  $\text{mV s}^{-1}$  voltage scan rates. The nearly rectangular shapes of the CVs over the various scan rates are consistent with the expected EDL capacitive properties for the hGO electrodes. The XPS results (vide supra) for the reduced graphenes shows a small amount of oxygen functional groups. These oxygen functional groups could be redox active and contribute faradaic activity during charge/discharge process. A small amount of Faradaic activity may lead to CVs that are not perfectly rectangular in shape. Compared to the CV studies of hGO in LiTFSI, the retention of rectangular over the  $-2\text{V}$  to  $2\text{V}$  voltage range indicates the stable electrochemical performance of hGO in the ionic liquid electrolyte (Fig. 6b). Even though the current responses shown in the CV diagrams in LiTFSI and EMITFSI are nearly the same, the cells with ionic liquid electrolyte exhibit EDL behavior over a larger voltage window. Thus,

higher energy and power performance in EMITFSI compared to LiTFSI can be expected. In order to determine the energy density and power density of both electrodes galvanostatic charge discharge measurements were conducted at different constant current densities. Fig. 6c shows nearly linear behavior of the discharge profile indicating the capacitive properties mainly arise from EDL and minor contributions from Faradaic capacitance. At  $0.5 \text{ A g}^{-1}$ , the hGO electrode delivered an energy density of  $43 \text{ W h kg}^{-1}$  (Fig. 6d). The specific capacitance recorded at this discharge rate was  $99 \text{ F g}^{-1}$ , which is higher than the specific capacitance of rGO ( $58 \text{ F g}^{-1}$ ). The energy density of  $30 \text{ W h kg}^{-1}$  was measured for rGO at  $0.5 \text{ A g}^{-1}$ . The energy density of hGO in the ionic liquid was much higher than that of the energy density exhibited in LiTFSI electrolyte. The power density of the hGO electrode at a constant current of  $10 \text{ A g}^{-1}$  was  $11.5 \text{ kW kg}^{-1}$  and  $8.8 \text{ kW kg}^{-1}$  for rGO. The Ragone plots for the devices fabricated with both rGO and hGO in organic and ionic liquid electrolytes are shown in Figs. 7a and 8. As in previous studies on graphene electrodes, both rGO and hGO binder-less paper electrodes exhibit higher energy and power densities than that of other type of commercially available energy storage devices (without considering the weight of the coin cell packaging).

As can be seen hGO delivers higher power density than that of rGO. However, in both electrolytes at higher energy densities, the power density of the rGO electrode drops much faster than that of hGO. At a given discharge current, the hGO electrodes can deliver both higher energy and power density in both electrolytes. The high power density of an electrode is directly related to the fast charge transfer kinetics involved in charge/discharge process. Based on electrochemical studies performed on the hGO and rGO electrodes, it would appear that the hGO electrode may have higher

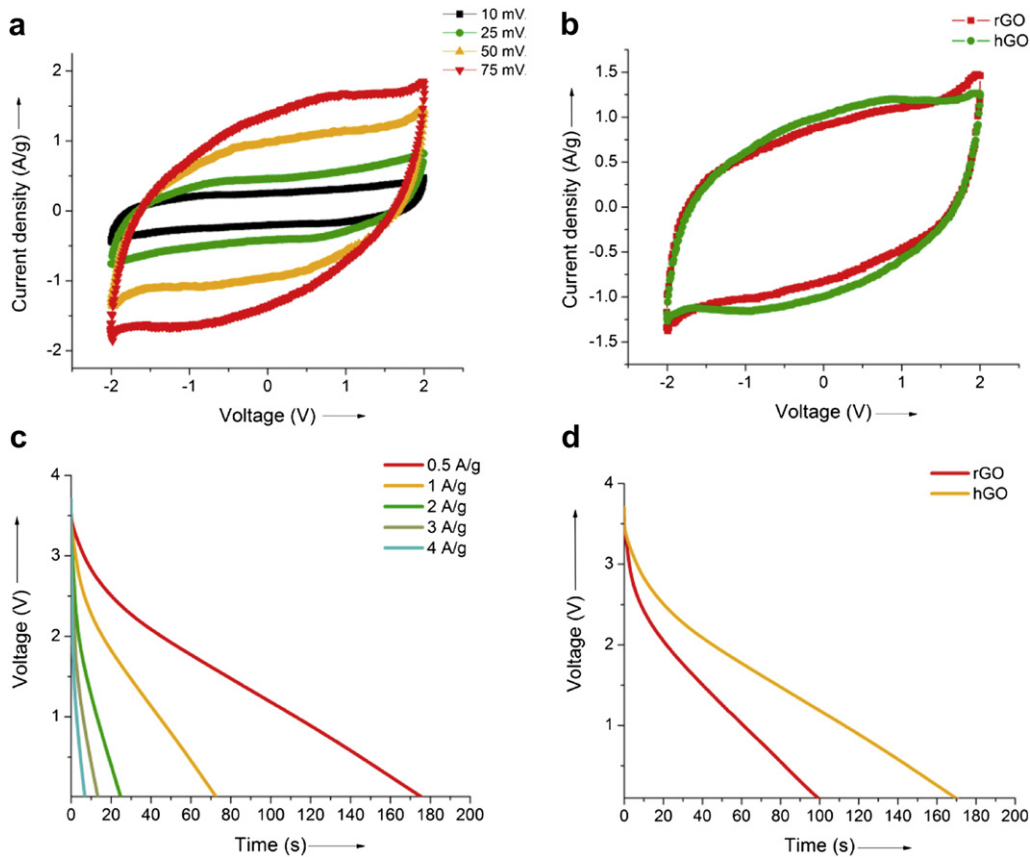


**Fig. 6.** (a) Cyclic voltammograms of the hGO paper electrode for various voltage scan rates in EMITFSI electrolyte. (b) Comparison of cyclic voltammograms of hGO and rGO acquired at  $25 \text{ mV s}^{-1}$ . (c) Galvanostatic discharging curves at  $0.5\text{--}4 \text{ A g}^{-1}$  current densities and (d) the comparison of discharge curves of hGO and rGO at  $0.5 \text{ A g}^{-1}$ .

ion mobility and less resistance to electron transport. Electrochemical impedance spectroscopy (EIS) can be used to understand the resistive components involved with electrochemical systems. Hence, the internal resistance parameters of the fabricated coin cell supercapacitors were evaluated using EIS. The Nyquist plots in Fig. 7b indicate ideal capacitive behavior of both rGO and hGO electrodes with a semi-circle at high-medium frequency and an inclined line at low frequency, which corresponds to charge transfer and diffusion respectively. The first intersection point on the real axis of the Nyquist spectrum in the high frequency region corresponds to the total resistance due to resistance from

electrolyte ( $R_s$ ), electrodes ( $R_e$ ) and the contacts ( $R_c$ ) between the electrode and current collector. The second intersection point on the real axis at medium frequency is associated with the interfacial contact capacitance ( $C_c$ ) and charge transfer resistance ( $R_{ch}$ ). In this semi-circle region only a small amount of charge-complexes can overcome the activation barrier and migrate (also called kinetic regime) [59]. The impedance spectra for both rGO and hGO in the organic electrolyte show lower total resistance for the assembled cells and charge transfer resistance than that of the ionic liquid. Generally, the higher viscosity associated with the ionic liquids creates resistance for ion mobility within the electrolytes. However,

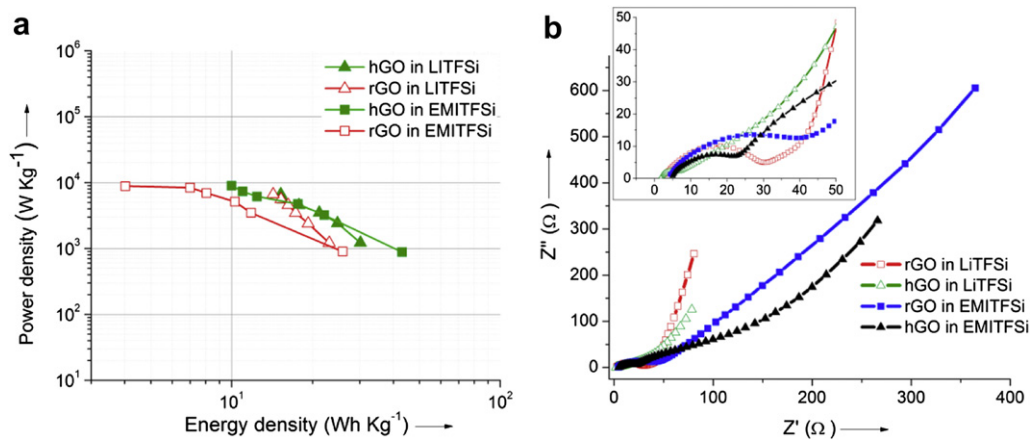


**Fig. 7.** (a) Ragone plot of hGO and rGO in organic (LiTFSI) and ionic liquid (EMITFSI) electrolytes and (b) corresponding impedance spectra of hGO and rGO in both electrolyte systems.

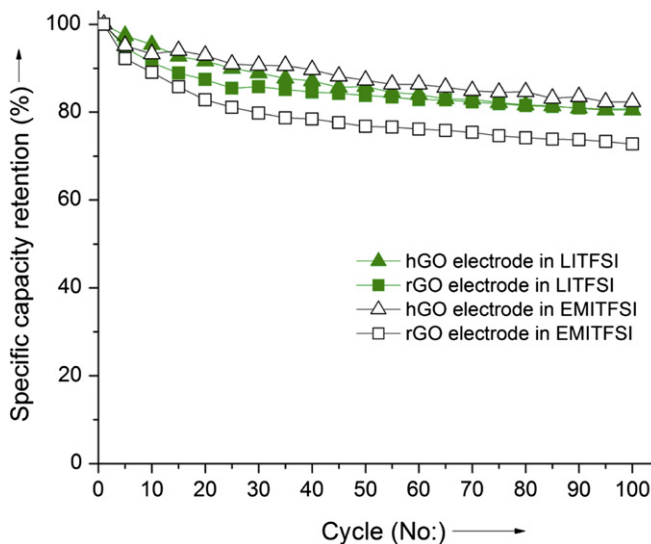


**Fig. 8.** Calculated retained capacity for 100 cycles at a charge discharge current density of  $0.5 \text{ A g}^{-1}$  for hGO and rGO electrodes in organic and ionic liquid electrolytes.

in both electrolytes, the charge transfer resistance for the hGO electrode was much lower than that of the rGO electrodes, indicating more efficient charge transfer kinetics compared to rGO. The reduced GO obtained by both methods results in a small amount of oxygen functional groups not converted. These functional groups may contribute Faradaic activity within the electrode [60]. Oxygen functional groups on reduced graphene have been electrochemically reduced at a potential of  $-0.75 \text{ V}$  (reference to reversible hydrogen electrode [RHE]) [61]. Therefore, during the charge discharge cycles these oxygen functional groups could also be electrochemically reduced to graphene and the amount of oxygen functional groups on hGO could be further decreased. The charge transfer resistance values, calculated by the difference between electrode resistance and total resistance, were  $30 \Omega$  for rGO and  $7.2 \Omega$  for hGO in LiTFSI and  $50 \Omega$  for rGO and  $25 \Omega$  for hGO in EMITFSI respectively. Moreover, the Nyquist plots for the cells prepared with LiTFSI showed linear region followed by semi-circle. Similar pattern was previously observed for CNT electrodes in  $\text{Li}^+$  based electrolytes [13,62]. The comparable power and energy density delivered within the short discharge time for hGO can be explained by the resistance associated with the charge discharge process. As suggested by Raman spectroscopy, the enhanced electronic conductivity of hGO may be due to the presence of larger  $\text{sp}^2$  domains. Although,  $\text{N}_2\text{H}_4$  is an efficient reducing agent for restoring the  $\text{sp}^2$  bonds in GO, the drastic nature of the reaction may cleave the  $\text{sp}^2$  domains and introduce heteroatoms such as N. In contrast, the alkaline deoxygenation process for hGO does not introduce heteroatoms. Moreover, the larger  $\text{sp}^2$  domains of hGO facilitate the fast charge transfer kinetics and support the electrochemical stability over charge and discharge cycles. In order to compare the cycling performance of the hGO electrodes with the rGO electrodes, the retention of specific capacitance over 100 continues cycles at a charge discharge rate of  $0.5 \text{ A g}^{-1}$  was calculated. At the 100th cycle, the specific charge retention for hGO and rGO electrodes were nearly equal in LiTFSI ( $\sim 80\%$ ). It is interesting to note that the hGO electrode in EMITFSI was much stable than that of for rGO (82% Vs 72%). This suggests that hGO electrodes are equally well suited for EDLC and Li ion batteries. Large  $\text{sp}^2$  domains with low charge transfer resistance may facilitate the adsorption of ions to create double layers at the electrode electrolyte interface in the EDLC configuration. Moreover, the stable high energy and power

performance of hGO in Li ion based electrolytes further confirms the potential use of hGO electrodes in Li ions batteries. Similar to the previous reports on graphene based electrodes, both hGO and rGO electrodes showed lower Coulombic efficiency (i.e. % ratio of charge to discharge capacity) during initial charge discharge cycling [53]. Initially, the hGO electrode showed a Coulombic efficiency of  $\sim 65\%$  and  $\sim 77\%$  in LiTFSI and EMITFSI, respectively. However, upon charging and discharging over 100 cycles, the Coulombic efficiency was enhanced to 78% in LiTFSI and 99.5% in EMITFSI. The high Coulombic efficiency of hGO in EMITFSI could be attributed to the effective formation of the electric double layer and a fast charge transfer process. The lower Coulombic efficiency of hGO in LiTFSI compared to EMITFSI may be due to the reversible Li ion intercalation between graphene sheets and the formation of  $\text{LiC}_6$ . Generally, the surface electrostatic charge adsorption and desorption rate in EDLC is much faster than the Li ion insertion and deinsertion reaction (Eq(1)). Despite the fact that the exact underlying mechanism for the restoring graphene properties and introducing large  $\text{sp}^2$  domains after alkaline hydrothermal treatment are unclear, the hGO performs better or equal than the hydrazine reduced rGO.

#### 4. Conclusion

We have demonstrated an alkaline hydrothermal process to deoxygenate GO, thus enabling the reduction of GO without using hydrazine as a reducing agent. The strong alkaline medium and hydrothermal conditions may cleave large oxidative debris attached to the GO surface to yield reduced GO. As a result of the alkaline hydrothermal treatment, oxygen functionalities were removed without introducing heteroatoms. The oxygen composition of the hGO was much smaller than that of the GO, suggesting that the degree of reduction of the alkaline hydrothermal treatment is similar to the conventional hydrazine reduction technique. It was also demonstrated that the hGO also forms flexible, freestanding, binder-free electrodes by vacuum filtration. Electrochemical properties of alkaline deoxygenated GO and hydrazine reduced GO was evaluated in both organic and ionic electrolyte. Compared to hydrazine reduced GO, the presence of larger  $\text{sp}^2$  domains was further supported by the lower charge transfer resistance obtained from EIS for the hGO electrode. Larger  $\text{sp}^2$  domains may enhance the charge transfer kinetics and provide short diffusion paths for electrons. The hGO electrodes exhibit ideal capacitive properties in both organic and ionic liquid electrolytes. The specific capacitance of hGO in organic (1M LiTFSI in acetonitrile) and ionic liquid (EMITFSI) electrolytes was  $\sim 145 \text{ F g}^{-1}$  and  $99 \text{ F g}^{-1}$  respectively. The hGO electrode delivered energy density of  $30 \text{ W h kg}^{-1}$  and power density of  $12.5 \text{ kW kg}^{-1}$  in the organic electrolyte and energy density of  $43 \text{ W h kg}^{-1}$  and power density of  $11.5 \text{ kW kg}^{-1}$  in the ionic liquid electrolyte, which is competitive with the hydrazine reduced GO electrode. In both electrolytes, the hGO electrode discharged faster than that of the rGO, while delivering the same amount of energy and power. Based on capacitive, energy and power performance, reduced GO prepared via alkaline hydrothermal process would be a feasible green route to obtain high quality graphene without using chemically hazardous strong reducing agents.

#### Acknowledgments

We would like to gratefully acknowledge the U.S Department of Energy (DE-EE004186) for financial support.

#### Appendix A. Supplementary material

Supplementary material associated with this article can be found, in the online version, at doi:10.1016/j.jpowsour.2012.04.059.

## References

- [1] A. Aric, P. Bruce, B. Scrosati, J.-M. Tarascon, W. Van Schalkwijk, *Nat. Mater.* 4 (2005) 366–377.
- [2] M. Winter, R. Brodd, *Chem. Rev.* 104 (2004) 4245–4269.
- [3] A. Burke, *J. Power Sources* 91 (2000) 37–50.
- [4] P. Simon, Y. Gogotsi, *Nat. Mater.* 7 (2008) 845–854.
- [5] E. Frackowiak, *Phys. Chem. Chem. Phys.* 9 (2007) 1774–1785.
- [6] A. Laforgue, P. Simon, J. Fauvarque, M. Mastragostino, F. Soavi, J. Sarrau, P. Lailier, M. Conte, E. Rossi, S. Saguatti, *J. Electrochem. Soc.* 150 (2003) A645–A651.
- [7] H. Zhang, W. Zhang, J. Cheng, G. Cao, Y. Yang, *Solid State Ionics* 179 (2008) 1946–1950.
- [8] C. Liu, Z. Yu, D. Neff, A. Zhamu, B. Jang, *Nano Lett.* 10 (2010) 4863–4868.
- [9] Y. Chen, X. Zhang, D. Zhang, P. Yu, Y. Ma, *Carbon* 49 (2011) 573–580.
- [10] G.A. Snook, P. Kao, A.S. Best, *J. Power Sources* 196 (2011) 1–12.
- [11] J.Y. Lee, K. Liang, K.H. An, Y.H. Lee, *Synth. Met.* 150 (2005) 153–157.
- [12] W.-C. Fang, *J. Phys. Chem. C* 112 (2008) 11552–11555.
- [13] S.D. Perera, B. Patel, N. Nijem, K. Roodenko, O. Seitz, J.P. Ferraris, Y. Chabal, K.J. Balkus, *Adv. Energy Mater.* 1 (2011) 936–945.
- [14] Y. Zhu, S. Murali, W. Cai, X. Li, J. Suk, J. Potts, J.R. Ruoff, *Adv. Mater.* 22 (2010) 3906–3924.
- [15] S. Vivekchand, C. Rout, K. Subrahmanyam, A. Govindaraj, C. Rao, *J. Chem. Sci.* 120 (2008) 9–13.
- [16] M. Stoller, S. Park, Z. Yanwu, J. An, R. Ruoff, *Nano Lett.* 8 (2008) 3498–3502.
- [17] Y. Wang, Z. Shi, Y. Huang, Y. Ma, C. Wang, M. Chen, Y. Chen, *J. Phys. Chem. C* 113 (2009) 13103–13107.
- [18] X. Yang, Y.-S. He, G. Jiang, X.-Z. Liao, Z.-F. Ma, *Electrochem. Commun.* 13 (2011) 1166–1169.
- [19] J.J. Yoo, K. Balakrishnan, J. Huang, V. Meunier, B.G. Sumpter, A. Srivastava, M. Conway, A.L. Mohana Reddy, J. Yu, R. Vajtai, P.M. Ajayan, *Nano Lett.* 11 (2011) 1423–1427.
- [20] H. Gwon, H.-S. Kim, K. Lee, D.-H. Seo, Y. Park, Y.-S. Lee, B. Ahn, K. Kang, *Energy Environ. Sci.* 4 (2011) 1277–1283.
- [21] Y. Zhu, S. Murali, M. Stoller, A. Velamakanni, R. Piner, R. Ruoff, *Carbon* 48 (2010) 2118–2122.
- [22] S. Stankovich, D. Dikin, R. Piner, K. Kohlhaas, A. Kleinhammes, Y. Jia, Y. Wu, S. Nguyen, R. Ruoff, *Carbon* 45 (2007) 1558–1565.
- [23] H. Wang, J. Robinson, X. Li, H. Dai, *J. Am. Chem. Soc.* 131 (2009) 9910–9911.
- [24] X.-Y. Peng, X.-X. Liu, D. Diamond, K. Lau, *Carbon* 49 (2011) 3488–3496.
- [25] W.S. Hummers, R.E. Offeman, *J. Am. Chem. Soc.* 80 (1958) 1339.
- [26] S. Park, S.J. An, J. Potts, A. Velamakanni, S. Murali, R. Ruoff, *Carbon* 49 (2011) 3019–3023.
- [27] H. Shin, K. Kim, A. Benayad, S. Yoon, H. Park, I. Jung, M. Jin, H. Jeong, J. Kim, J. Choi, Y. Lee, *Adv. Funct. Mater.* 19 (2009) 1987–1992.
- [28] C.-Y. Su, Y. Xu, W. Zhang, J. Zhao, A. Liu, X. Tang, C.-H. Tsai, Y. Huang, L.-J. Li, *ACS Nano* 4 (2010) 5285–5292.
- [29] X. Fan, W. Peng, Y. Li, X. Li, S. Wang, G. Zhang, F. Zhang, *Adv. Mater.* 20 (2008) 4490–4493.
- [30] J. Rourke, P. Pandey, J. Moore, M. Bates, I. Kinloch, R. Young, R.N. Wilson, *Angew. Chem. Int. Ed.* 50 (2011) 3173–3177.
- [31] A. Baldacci, R. Dugas, P. Taberna, P. Simon, D. Plée, M. Mastragostino, S. Passerini, *J. Power Sources* 165 (2007) 922–927.
- [32] D. Dreyer, S. Murali, Y. Zhu, R. Ruoff, C. Bielawski, *J. Mater. Chem.* 21 (2011) 3443–3447.
- [33] I. Moon, J. Lee, R. Ruoff, H. Lee, *Nat. Commun.* 1 (2010).
- [34] X.-F. Wang, Q.-Y. Qian, F.-B. Wang, X.-H. Xia, *ACS Nano* 3 (2009) 2653–2659.
- [35] Y.H. Ng, I.V. Lightcap, K. Goodwin, M. Matsumura, P.V. Kamat, *J. Phys. Chem. Lett.* 1 (2010) 2222–2227.
- [36] X. Wang, L. Zhi, K. Müllen, *Nano Lett.* 8 (2008) 323–327.
- [37] Q. Wu, Y. Xu, Z. Yao, A. Liu, G. Shi, *ACS Nano* 4 (2010) 1963–1970.
- [38] X. Dong, C.-Y. Su, W. Zhang, J. Zhao, Q. Ling, W. Huang, P. Chen, L.-J. Li, *Phys. Chem. Chem. Phys.* 12 (2010) 2164–2169.
- [39] D. Dreyer, S. Park, C. Bielawski, R. Ruoff, *Chem. Soc. Rev.* 39 (2010) 228–240.
- [40] K.N. Kudin, B. Ozbas, H.C. Schniepp, R.K. Prud'homme, I. Aksay, R. Car, *Nano Lett.* 8 (2007) 36–41.
- [41] Z. Ni, Y. Wang, T. Yu, Z. Shen, *ChemInform* 41 (2010).
- [42] B.Z. Jang, C. Liu, D. Neff, Z. Yu, M.C. Wang, W. Xiong, A. Zhamu, *Nano Lett.* 11 (2011) 3785–3791.
- [43] T. Bhardwaj, A. Antic, B. Pavan, V. Barone, B.D. Fahlman, *J. Am. Chem. Soc.* 132 (2010) 12556–12558.
- [44] K. Haubner, J. Murawski, P. Olk, L. Eng, C. Ziegler, B. Adolphi, E. Jaehne, *Chem. Phys. Chem.* 11 (2010) 2131–2139.
- [45] C. Mattevi, G. Eda, S. Agnoli, S. Miller, K. Mkhoyan, O. Celik, O.D. Mastrogiovanni, C. Cranozzi, E. Carfunkel, M. Chhowalla, *Adv. Funct. Mater.* 19 (2009) 2577–2583.
- [46] Y. Matsumoto, M. Koinuma, S. Kim, Y. Watanabe, T. Taniguchi, K. Hatakeyama, H. Tateishi, S. Ida, *ACS Appl. Mater. Sci.* 2 (2010) 3461–3466.
- [47] B. Zhao, P. Liu, Y. Jiang, D. Pan, H. Tao, J. Song, T. Fang, W. Xu, *J. Power Sources* 198 (2012) 423–427.
- [48] D.S. Knight, W.B. White, *J. Mater. Res.* 4 (1989) 385–393.
- [49] A. Ferrari, J. Meyer, V. Scardaci, C. Casiraghi, M. Lazzeri, F. Mauri, S. Piscanec, D. Jiang, K. Novoselov, S. Roth, A. Geim, *Phys. Rev. Lett.* 97 (2006) 187401–187405.
- [50] M. Lezanska, P. Pietrzyk, Z. Sojka, *J. Phys. Chem. C* 114 (2010) 1208–1216.
- [51] Y. Xu, K. Sheng, C. Li, G. Shi, *ACS Nano* 4 (2010) 4324–4330.
- [52] X. Zhang, Z. Sui, B. Xu, S. Yue, Y. Luo, W. Zhan, B. Liu, *J. Mater. Chem.* 21 (2011) 6494–6497.
- [53] A. Abouimrane, O. Compton, K. Amine, S. Nguyen, *J. Phys. Chem. C* 114 (2010) 12800–12804.
- [54] T. Kim, H. Lee, M. Stoller, D. Dreyer, C. Bielawski, R. Ruoff, K. Suh, *ACS Nano* 5 (2011) 436–442.
- [55] E. Yoo, J. Kim, E. Hosono, H.-S. Zhou, T. Kudo, I. Honma, *Nano Lett.* 8 (2008) 2277–2282.
- [56] K. Tatsumi, N. Iwashita, H. Sakaebi, H. Shioyama, S. Higuchi, A. Mabuchi, H. Fujimoto, *J. Electrochem. Soc.* 142 (1995) 716–720.
- [57] C. Largeot, C. Portet, J. Chmiola, P.-L. Taberna, Y. Gogotsi, P. Simon, *J. Am. Chem. Soc.* 130 (2008) 2730–2731.
- [58] V. Borgel, E. Markevich, D. Aurbach, G. Semrau, M. Schmidt, *J. Power Sources* 189 (2009) 331–336.
- [59] K. Hung, C. Masarapu, T. Ko, B. Wei, *J. Power Sources* 193 (2009) 944–949.
- [60] Y. Harima, S. Setodji, I. Imae, K. Komaguchi, Y. Ooyama, J. Ohshita, H. Mizota, J. Yano, *Electrochim. Acta* 56 (2011) 5363–5368.
- [61] Y. Shao, J. Wang, M. Engelhard, C. Wang, Y. Lin, *J. Mater. Chem.* 20 (2010) 743–748.
- [62] Z. Yang, S. Sang, K. Huang, H.-Q. Wu, *Diamond Relat. Mater.* 13 (2004) 99–105.